Radar and Lidar Observations for Determining Particle Radii

Victoria Pinnegar, Callum Dewsnap

December 2021

1 Introduction

The use of radar (**ra**dio **d**etection **a**nd **r**anging) and lidar (**li**ght **d**etection **a**nd **r**anging) in the viewing and categorizing of the atmosphere has been in popular use since the 20th century. The experimental use of both instruments in conjunction allows for easy observation of particle radius. This allows for easy characterization of particles in the troposphere and stratosphere for climatology surveys (Bourdages et al., 2009).

1.1 Cloud Formation

The concept of cloud formation, in terms of the micro-physical processes, is very complicated. What is utilized in this simulation does not rely on the formation potential of a cloud, but rather the situational factors after a cloud has formed.

The variables of cloud formation that this study explores are the state variables of the atmosphere. Specifically, the atmospheric temperature and pressure which produce some area of increased or decreased particle density. Considering this, the model used in this experiment simulates areas of lowered temperature, where cloud condensation would occur more easily due to lower saturation vapour pressure (Ahrens, 2008). Ideally, the conditions follow that of the ideal gas such that

$$T = \frac{P}{nk}, \tag{1}$$

where an increased number density n will lower the temperature T and allow for easier condensation due to lower saturation vapour pressure. Or alternatively a decrease in pressure P causes an decrease in temperature, allowing for easier condensation. Here, k is the Boltzmann constant.

Just as indicated in this thought experiment, cloud formation does occur in low pressure zones as dictated by large scale atmospheric circulation. The three cells, namely the Hadley Cell, Polar Cell and Ferrell Cell, dictate the tropospheric air circulation across the earth's surface, which therefore dictate the formation of low and high pressure zones (Hadley).

These low pressure systems have wind blowing towards the lower pressure, where the air converges and water vapour is pushed up into the atmosphere where it condenses into cloud nuclei. Additionally, the low pressure systems turn counterclockwise due to the Coriolis effect (The highs and lows of air pressure).

1.2 Lidar and Radar

Lidar, in the most basic sense, utilizes backscattered photons to determine certain optical properties and structure of the atmosphere (Geisinger et al., 2017). Radar follows similar principles at much longer wavelengths and different set ups (Bourdages et al., 2009). Both can be broken down into their general equation for functionality.

1.2.1 Lidar

The returned power for a lidar can be defined here as

$$P(R,\lambda) = P_0 \frac{c\tau}{2} A\eta \frac{O(R)}{R^2} \beta(R,\lambda) \exp\left[-2\int_0^R \alpha(r,\lambda)dr\right]. \tag{2}$$

Here we have the average pulse power P_0, the temporal pulse length $c\tau/2$, the area of the receiver A, the detector efficiency η, the overlap function $O(r)$, the range R, the backscatter β, and the extinction α (Geisinger et al., 2017).

1.2.2 Radar

The average received power for the radar is defined by

$$p_r = \frac{\pi^5 P_t G^2 \lambda^2 |K|^2 Z_e}{(4\pi)^3 l \lambda^4 R^4}. \tag{3}$$

Here we have the average power of a single laser pulse P_t, the gain G, the loss l, the wavelength λ, the range R, and the reflectivity Z_e (Donovan and van Lammeren, 2001). When comparing the radar to the lidar in measurements, reflectivity and backscatter are the variables directly proportional to one another. Reflectivity can be converted into backscatter using

$$\beta = Z_e K^2 \frac{\pi^4}{4\lambda^4} = Z_e \left(\frac{n^2-1}{n^2+2}\right)^2 \frac{\pi^4}{4\lambda^4}, \tag{4}$$

where n is the index of refraction. This also differs from a traditional representation of radar backscatter since it converts it into a representation analogous to lidar backscatter. It is off by a division factor of 4π which puts it in units of $\mathrm{sr}^{-1}\mathrm{m}^{-1}$ (Donovan and van Lammeren, 2001).

1.3 Backscatter

1.3.1 Rayleigh

Radiation interacts with the atmosphere as it travels and can be scattered or absorbed. The scattering that occurs depends on the wavelength of the incoming radiation, size, shape and composition of the particle. The possible types of scattering occur depending on a function called the size parameter given by

$$x = \frac{2\pi r}{\lambda}. \tag{5}$$

Here, r is the particle radius and λ is the wavelength of the observation. (Meteo 300). The possible types of backscatter, as dictated by Figure 1, are Rayleigh, Mie and geometric.

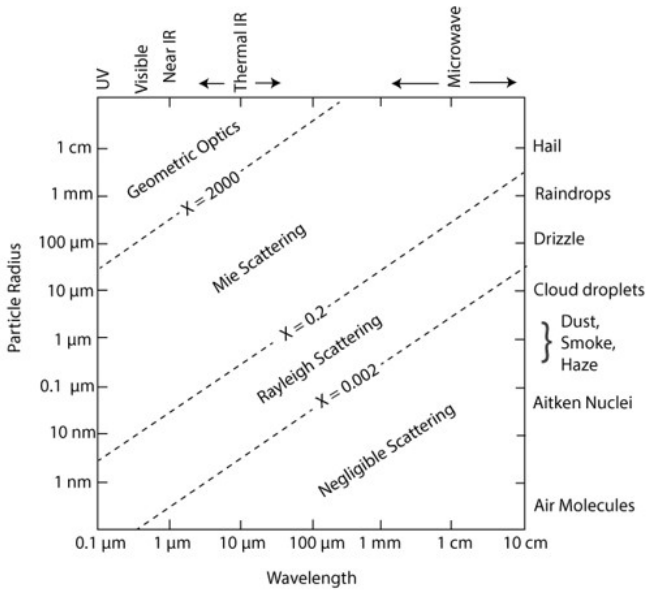

Figure 1: The regimes within which each type of scattering dominates.(Meteo 300).

Geometric follows the rules of typical optics while the other two scattering functions are complicated approximations based off of Maxwell's equations. A typical lidar will interact with air molecules, or molecular backscatter in the Rayleigh regime, while the particulate backscatter (aerosol or clouds) are more likely in the Mie regime (Abud, 2018). Radar wavelengths are much longer and therefore will interact with particulates in the Rayleigh regime (Donovan and van Lammeren, 2001).

As previously discussed, the radar will be within the Rayleigh regime for the observable particulates such as water cloud nuclei and dust/other aerosols. Therefore, the backscatter coefficient is defined as

$$\beta_{\text{radar}} = N_0 \left\langle \left(\frac{d\sigma_{\text{radar}}}{d\Omega} \right)_{\pi} \right\rangle = N_0 \left(\frac{2\pi}{\lambda_{\text{radar}}} \right)^4 \frac{1}{|K^2|} \left\langle r^6 \right\rangle . \tag{6}$$

(Donovan and van Lammeren., 2001). Anything smaller than aerosol particles for the radar at the simulated wavelength (8.6 mm) becomes negligible.

1.3.2 Mie

Mie scattering will be the typical particulate scattering type for the lidar backscatter at the simulated wavelength (532 nm). Mie scattering is defined as

$$\beta = N\pi r^2 Q_{\text{back}}, \tag{7}$$

where N is the number density, r is the time averaged particle radius, and Q_{back} is the backscatter efficiency. Q_{back} is defined by the Bernoulli solution given by

$$Q_{\text{back}} = \frac{1}{x^2} \sum_{n=1}^{\infty} \left| (2n+1)(-1)^{-n}(a_n + b_n) \right|^2 . \tag{8}$$

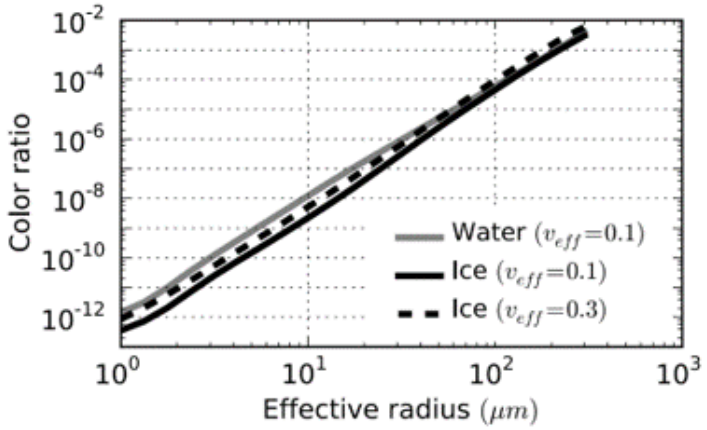

Figure 2: The colour ratio as a function of the effective radius (Bourdages et al. 2009).

1.4 Colour Ratio

Taking the colour ratio of both the radar and the lidar produces

$$\frac{\beta_{\text{radar}}}{\beta_{\text{lidar}}} = \frac{\left(\frac{2\pi}{\lambda_{\text{radar}}}\right)^4 \frac{1}{|K^2|} \langle r^6 \rangle}{\pi \langle r \rangle^2 Q_{\text{back}}} \tag{9}$$

(Bourdages et al., 2009). This relation is proportional to to the effective radius of the particle,

$$\frac{\beta_{\text{radar}}}{\beta_{\text{lidar}}} \propto R'_{\text{eff}} = \left(\frac{\langle r^6 \rangle}{\langle r^2 \rangle}\right)^{\frac{1}{4}} \tag{10}$$

(Donovan and van Lammeren. 2001). The relationship between the two is linearly proportional as seen in Figure 2.

The effective radius defines important parameters in water clouds as explained by Foot (1988)

$$R_{eff} \approx \frac{3}{2} \frac{\text{LWC}}{\rho_w \alpha_{\text{vis}}} \tag{11}$$

where ρ_w is the density of water, LWC is the liquid water content and α_{vis} is the extinction coefficient for the visible spectrum.

2 Simulation

The model objectives were to view the observation of actual particle radius versus the effective particle radius utilizing a lidar and radar in conjunction. Using the simulated atmosphere, a backscatter based off of radius and wavelength is determined for both lidar and radar using Equations 6 and 7.

2.1 Atmosphere Simulation

The simulated atmosphere produces an interpolated density as a function of time and height. It generates a model atmosphere by creating a distribution of $P/T = nk$ which randomly varies over time. Here, P is the pressure, T is temperature, n is the

number density, and k is the Boltzmann constant. The initial distribution is a Gaussian which varies every hour for 24 hours. This variation is calculated by shifting each of the mean height and standard deviation by a randomly-determined value through the use of another normal distribution. The standard deviation is set to preferentially increase, thus causing the cloud to typically diffuse over time. The mean height of the distribution is limited to be higher than 800 metres and the standard deviation of the height's time variation is constrained to be greater than one third of the initial standard deviation at all times. The time bins between the hour marks are determined by performing a two-dimensional linear interpolation. The number of particles within the distribution is kept at constant at all times. The dispersion over time models eddy diffusion, although occurs randomly by lowering the peak of the Gaussian and spreading the distribution. This does not alter the background density, just the density of the injected cloud of water or aerosol. The range is alterable, but for the purposes of this experiment, it goes up to 10 km. Additionally, each particle is given some randomized radius based off of the density profile as it moves through the lidar/radar field of view.

2.2 Instrument Properties

The instruments simulated in this program are based off of the Arctic High Spectral Lidar (AHSRL) and the Millimeter-wave Cloud Radar (MMCR) taken from Bourdages et al. (2009). They both are present at the Zero-altitude PEARL Auxiliary Laboratory. The wavelengths for both instruments were taken for the simulation (AHSRL: 532nm, MMCR: 8.6mm), while the spatial and temporal resolutions were altered to fit a simulated space. The temporal resolution of both instruments became 1 minute and the spatial resolution became 5m, although both values can be altered by the user.

3 Results

The simulation has a choice to run with either a water cloud distribution or an aerosol distribution. For the lidar, the type of scattering is dependent on the particle size, and for radar either Rayleigh or Mie can be chosen.

3.1 Water Cloud

Figure 3 shows the first simulated atmosphere for a water cloud. The background air particles have a typical radii of around 1 nm, while the water molecules size distribution follows Bourdages et al. (2009) (On the order of 1-10 μm). The complex refractive index for water is also taken from Bourdages et al. (2009) at 1.33 for lidar and $5+2.5i$ for radar at a temperature of 293 K. Using these refractive indexes, the theoretical backscatter from the AHSRL and MMCR are viewed.

4.

The raw backscatter for both the lidar and the radar are presented here in Figure 4. Given the known particle radii injected into the simulation and the relationship between colour ratio and effective radii, the ratio of the radar (Rayleigh) and the lidar should produce a linear relationship.

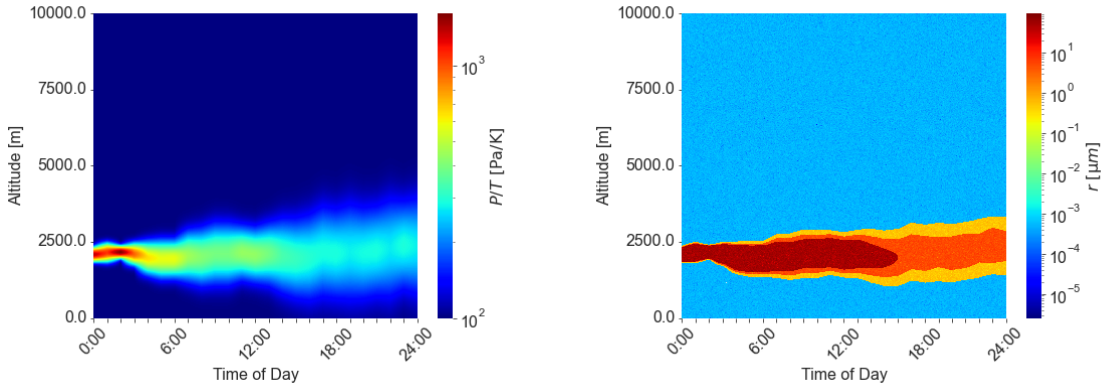

(a) Water cloud

(b) Particle radius distribution

Figure 3: Example of randomly generated water cloud atmosphere with the corresponding particle radius distribution.

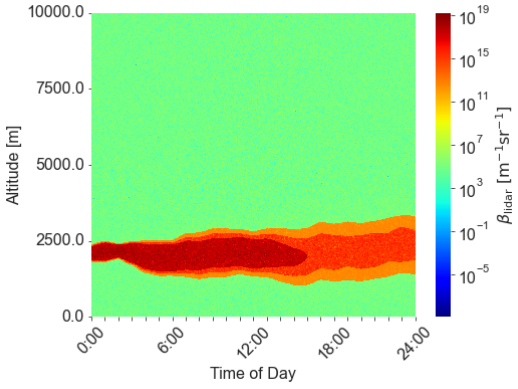

(a) Lidar backscatter

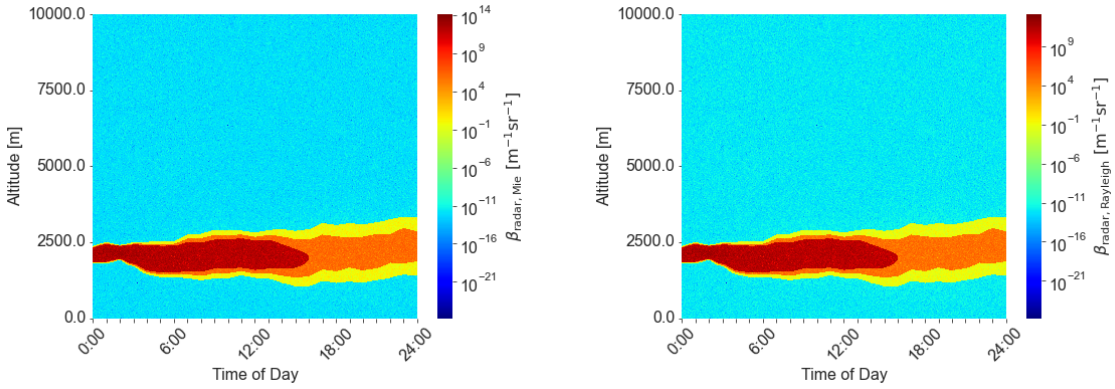

(b) Radar backscatter (Mie)

(c) Radar backscatter (Rayleigh)

Figure 4: Corresponding backscatter measurements of water cloud atmosphere shown in Figure 3.

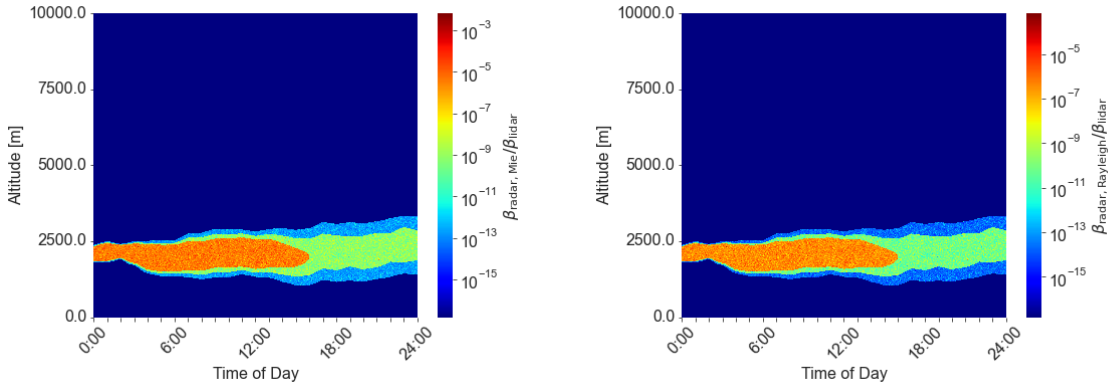

(a) Colour ratio for Mie scattering

(b) Colour ratio for Rayleigh scattering

Figure 5: Corresponding colour ratio measurements for the backscatters calculated in Figure 4.

3.2 Aerosol

The Aerosol viewing follows the same principles as the water cloud, except with a different radii distribution for dust and different refractive indexes. The radii distribution is between 0.1-1 μm, with a constant air molecule background on the order of 1 nm. The refractive indexes used for the aerosol are 1.0004478 for lidar and 1.0842 for radar. The refractive indices are assumptions based off of the molecular gas CH_4. A more accurate refractive index would be easily found for lidar wavelengths ($\sim$1.4) but reaching radar wavelengths is atypical(Juranyi 2019). A typical refractive index in the mm range would be complex, although not for this simulation. Figure 6 represents the randomly generated atmosphere for the aerosol measurement. It disperses over time as a function of gradual Gaussian diffusion representing Fick's first law. Fick's first law is given by

$$J = -D\frac{d\phi}{dx}, \tag{12}$$

where J is the diffusion flux, D is the diffusion coefficient, ϕ is the concentration, and x is the position (Thompson, 2006). Additionally, the background backscatter represented in both the lidar and radar plots seems to have a much higher scattering magnitude than the aerosol injected. This is not typical in an actual physical environment but does not effect the relevant area (within the aerosol cloud). The cause of this much stronger scatter is unknown, but potentially is due to the change of refractive index from the the aerosol to a typical air value (n = 1.000293).

4 Discussion

4.1 Water Cloud

The colour ratios of the water cloud, shown in Figure 5, can be directly corroborated by the studies done by Bourdages et al., (2009). The typical colour ratio viewed by that study were between $10^{-9} - 10^{-6}$ for a Mixed-Phase Cloud Water Droplet. As viewed by simulation, the Mie scattering used for radar gives values between the expected ratio, though do not follow the physical scattering expectation for the particle size. The

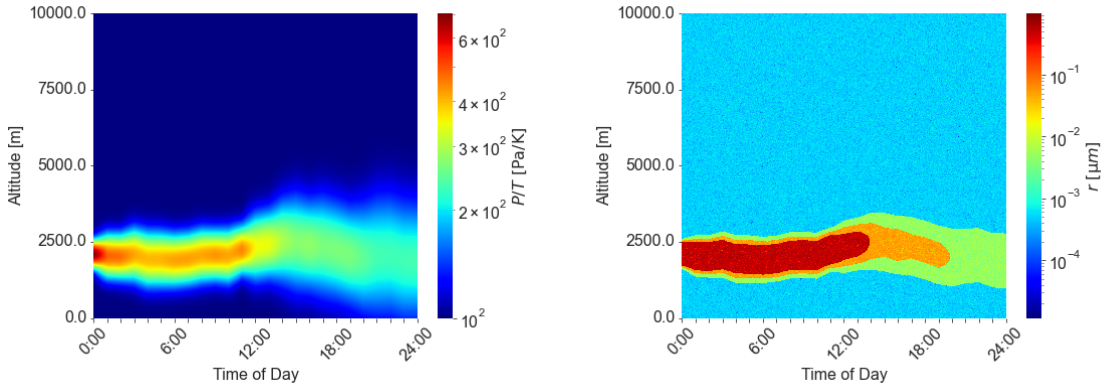

(a) Aerosol cloud

(b) Particle radius distribution

Figure 6: Example of randomly generated aerosol cloud atmosphere with the corresponding particle radius distribution.

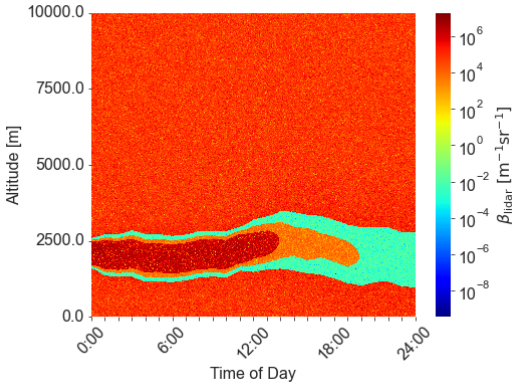

(a) Lidar backscatter

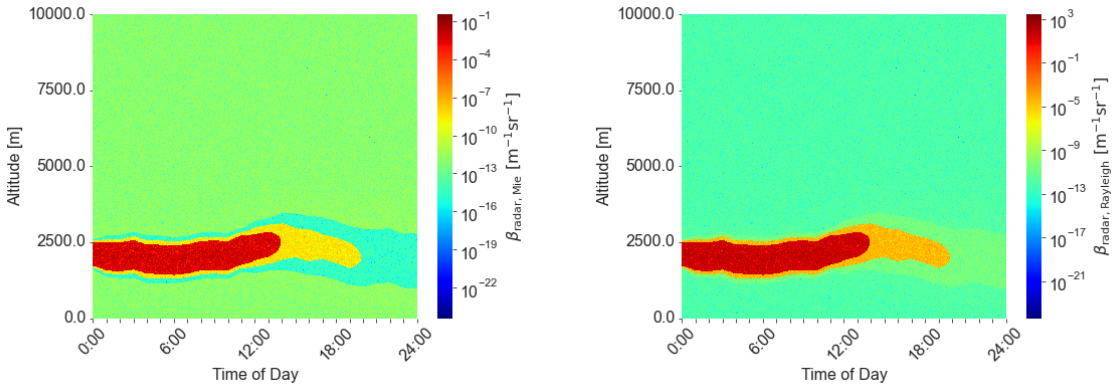

(b) Radar backscatter (Mie)

(c) Radar backscatter (Rayleigh)

Figure 7: Corresponding backscatter measurements of aerosol cloud atmosphere shown in Figure 6.

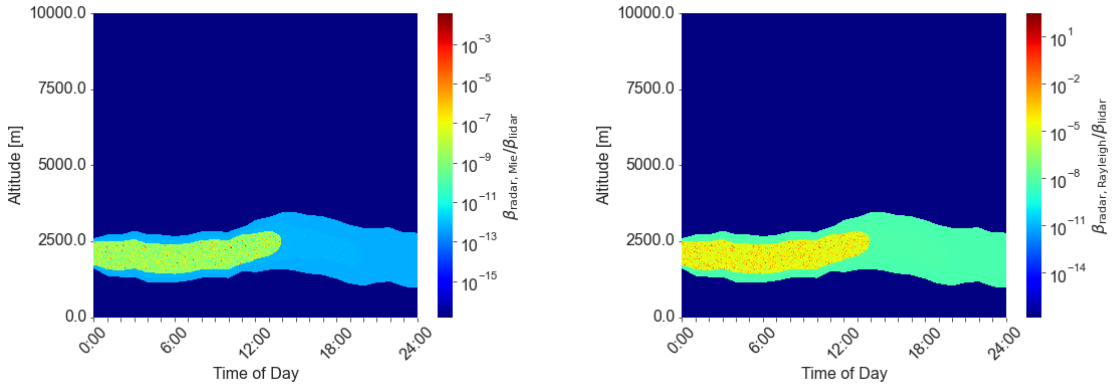

(a) Colour ratio for Mie scattering

(b) Colour ratio for Rayleigh scattering

Figure 8: Corresponding colour ratio measurements for the backscatters calculated in Figure 7.

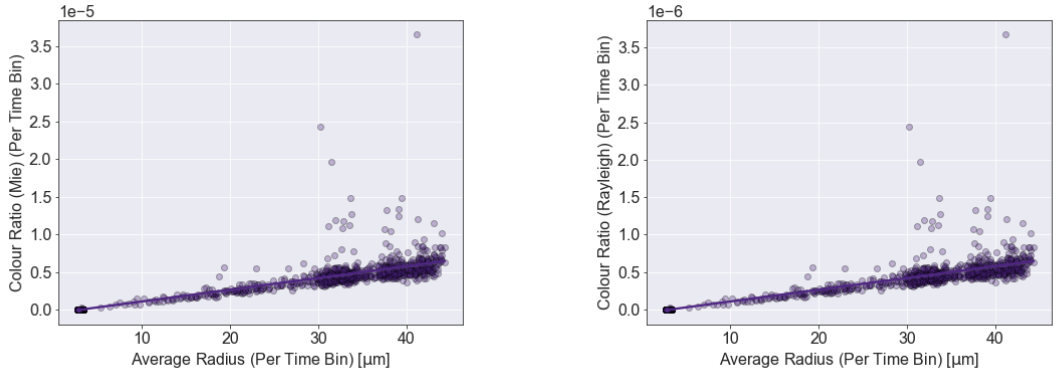

(a) Colour ratio (Mie) versus particle radius

(b) Colour ratio (Rayleigh) versus particle radius

Figure 9: Average colour ratio versus average particle radius for water cloud distribution given in Figure 3. Each point represents a time bin. In this case, each bin is one minute for a total of 24 hours.

Rayleigh scattering (Figure 5b) also shows a distribution similar to the mixed phase cloud water droplets viewed by Bourdages et al., (2009).

Bourdages additionally cites the effective radius for this $10^{-9} - 10^{-6}$ distribution to be $5 - 40\mu$m. Using Equation 10 to determine the proportional relationship, the fourth root of the colour ratio was taken to determine the approximate relationship between the effective radius and the colour ratio of the particulate. Figures 9 and 10 show the colour ratio and effective radius versus the simulated particle radius. Note that the effective radius is only defined when the radar is selected to use Rayleigh scattering and not for Mie scattering as the radii fully cancel and the colour ratio is independent of the radii distribution.

By taking the fourth root of the colour ratio given by Equation 9, it produces the effective radius multiplied by a scaling factor (A_{eff}) of

$$A_{\text{eff}} = \left(\frac{\left(\frac{2\pi}{\lambda_{\text{radar}}}\right)^4 \frac{1}{|K^2|}}{\pi Q_{\text{back}}} \right)^{\frac{1}{4}}. \tag{13}$$

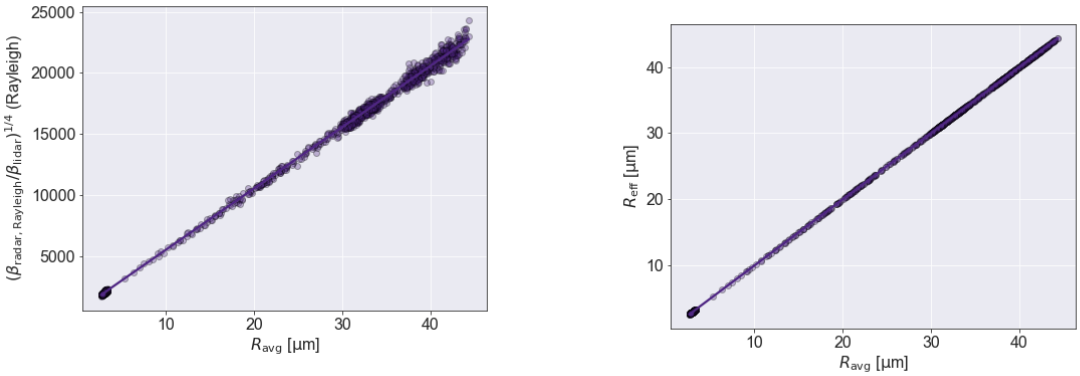

(a) Average $(\beta_{\text{radar}}/\beta_{\text{lidar}})^{1/4}$ versus average radius

(b) Effective radius versus average particle radius

Figure 10: Determination of average effective radius versus average particle radius for water cloud distribution given in Figure 3. Each point represents a time bin. In this case, each bin is one minute for a total of 24 hours.

The dependence of effective radius on colour ratio therefore becomes

$$\left(\frac{\beta_{\text{radar}}}{\beta_{\text{lidar}}}\right)^{1/4} = A_{\text{eff}} R'_{\text{eff}} = \left(\frac{\left(\frac{2\pi}{\lambda_{\text{radar}}}\right)^4 \frac{1}{|K^2|}}{\pi Q_{\text{back}}}\right)^{\frac{1}{4}} \left(\frac{\langle r^6 \rangle}{\langle r \rangle^2}\right)^{\frac{1}{4}}. \tag{14}$$

By dividing out A_{eff}, the effective radius will be exactly equal to the time averaged radius injected into the system. Figure 10b represents this calculation and shows the obvious 1:1, with the full elimination of the scale factor. The effective radius falls within the range of $5 - 40\mu$m estimated for spherical water droplets (Bourdages et al., 2009).

The study done by Mishchenko et al. (2002) utilizes the effective variance alongside the effective radius as the colour ratio was shown to be relatively insensitive to the particle distribution as shown by Bourdages et al. (2009). The typical particle distribution assumption for Bourdages et al. (2009) and Donnovan & van Lammeren (2001) is a gamma distribution

$$n(r) = \frac{N_0}{R_m} \frac{1}{\Gamma(\gamma)} \left(\frac{r}{R_m}\right)^{\gamma-1} \exp(-r/R_m) \tag{15}$$

This variance was kept at a max of 25% systematic error for Bourdages et al. (2009), which is what was maintained for this simulation.

4.2 Aerosol

Unlike Bourdages et al., (2009), this simulation also investigated aerosol-like particles to determine their effective radius as well. The relevant particle radii varied between 10^{-10} m for air and 0.4 μm as a maximum for the aerosol. The hypothesized colour ratio for aerosol was taken to be between the values of $10^{-12} - 10^{-9}$ and confirmed by the Figure 8. The minimum colour ratio value was taken from the typical value of air molecules from Bourdages et al., (2009). The max value was taken similarly as anything

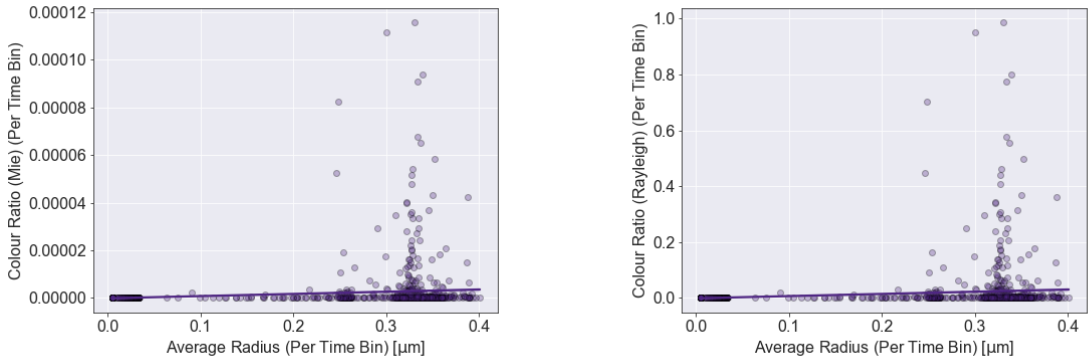

(a) Colour ratio (Mie) versus particle radius (b) Colour ratio (Rayleigh) versus particle radius

Figure 11: Average colour ratio versus average particle radius for aerosol cloud distribution given in Figure 6. Each point represents a time bin. In this case, each bin is one minute for a total of 24 hours.

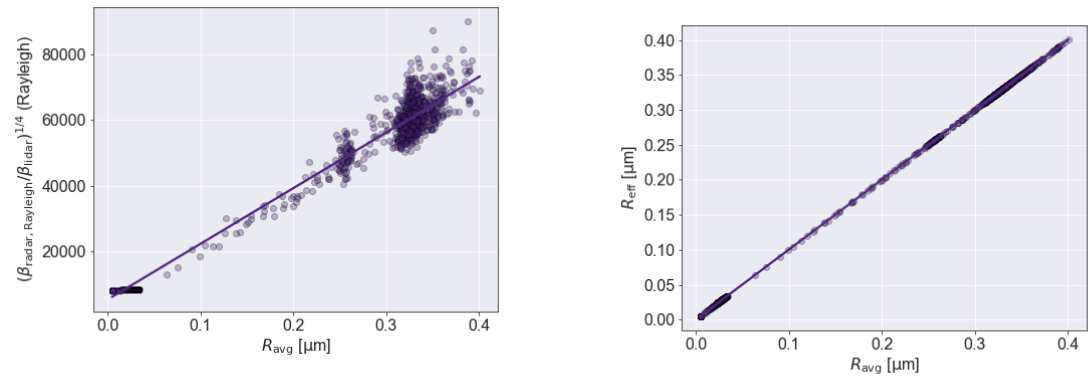

(a) Average $(\beta_{\text{radar}}/\beta_{\text{lidar}})^{1/4}$ versus average radius (b) Effective radius versus average particle radius

Figure 12: Determination of average effective radius versus average particle radius for aerosol cloud distribution given in Figure 6. Each point represents a time bin. In this case, each bin is one minute for a total of 24 hours.

smaller than a water droplet in the atmosphere. The colour ratio with the Mie scattering is much different for these particles, as it broaches the levels of negligible scattering. As previously mentioned, this is due to the ratio becoming independent of radius. Figure 11 and 12 show the colour ratio and average effective radius versus the average simulated radius.

As seen with the effective cloud radii, the effective aerosol radii produces a linear 1:1 relationship after applying the division of the scale factor shown by Equation 13.

5 Conclusions

The calculation of the effective radius with our method produces the exact inputted average radius. The issue with applying this method to an observed atmospheric environment comes with the need for a very accurate forward model. Without accurate representation of the refractive indexes and density distribution, the final effective radius will not produce a physically relevant answer. The application of the Optimal Estimation method to this forward model to determine the effective radius may allow for this to be applied to an observed atmosphere.

The obvious theoretical answer to the determination of the effective radii was for the inputted radii to be outputted. In other studies variations on this simulation, the backscattering from the lidar was slightly changed to match the situation. In Donovan & van Lammeren (2001), the lidar backscatter approached the boundary of geometric scattering

$$\beta = N\pi r^2 Q_{\text{back}} \approx 2\pi\langle r^2\rangle \tag{16}$$

where the total scattering for a spherical scatterer became two times its cross-sectional area. Additionally, the issue with the Mie scattering comes in the formulation of the equation. There is an assumption that radius is already known in the simulation formulation that is due to the calculation for the backscatter efficiency. The backscatter efficiency has a value of $\frac{1}{r^2}$ that would theoretically cancel out with the additonal r^2 in the equation, which leaves the only use of the radius in the determination of the coefficients, a_n and b_n. These are expressed

$$a_n = \frac{\psi_n'(y)\psi_n(x) - m\psi_n(y)\psi_n'(x)}{\psi_n'(y)\zeta_n(x) - m\psi_n(y)\zeta_n'(x)} \tag{17}$$

$$b_n = \frac{m\psi_n(y)\psi_n'(x) - \psi_n'(y)\psi_n(x)}{m\psi_n(y)\zeta_n'(x) - \psi_n'(y)\zeta_n(x)} \tag{18}$$

where x is the size parameter, y is mx (refractive index and size parameter), $\psi_n(z) = zj_n(z)$ and $\zeta_n(z) = zh_n^{(2)}$, where $j_n(z)$ and $h_n^{(2)}$ are both spherical Bessel functions (Adam, 2005).

The Donovan & van Lammeren (2001) formulation of the effective radius is the equation used in this simulation, although the effective radius based off of Mie scattering is

$$r_{\text{eff}} = \frac{\int_0^\infty n(r)r^3dr}{\int_0^\infty n(r)r^2dr} \tag{19}$$

with r as radius and n(r) as number density. The radius is also associated with the smallest dimension of the particle as defined by Bourdages et al. (2009).

The next steps to expand on this project would be to apply the simulation as a forward model onto a randomized backscatter. The potential for this to be completed using

optimal estimation method (OEM) would create an important tool for climatological surveyors with co-located instruments. Additionally, due to the use of a Gaussian number density distribution versus the Gamma number density distribution, the actual difference between the colour ratios due to this variation should be investigated. As mentioned by Bourdages et al. (2009), the colour ratio shouldn't be sensitive to the distribution type and most likely will produce the same answer. The final step for the program would be to optimize and apply it as a forward model for observational measurements. Overall, this method provides an accurate effective radius but only when using a highly accurate forward model to determine the A_{eff}.

6 References

Abud, M. M. (2018). Measure of backscatter for small particles of atmosphere by lasers. Journal of Physics: Conference Series, 1003, 012079. https://doi.org/10.1088/1742-6596/1003/1/012079

Adam, M. (2005). DEVELOPMENT OF LIDAR TECHNIQUES TO ESTIMATE ATMOSPHERIC OPTICAL PROPERTIES . Jscholarship. Retrieved from https://jscholarship.library.jhu.edu/bitstream/handle/1774.2/851/mariana_thesis.pdf.

Bourdages, L., Duck, T. J., Lesins, G., Drummond, J. R., & Eloranta, E. W. (2009). Physical properties of high Arctic tropospheric particles during winter. Atmospheric Chemistry and Physics, 9(18), 6881–6897. https://doi.org/10.5194/acp-9-6881-2009

Byhsotr, P. (2021, December 4). How plains tribes predicted The weather. Homestead on the Range. Retrieved December 8, 2021, from https://homesteadontherange.com/2020/07/29/how-plains-tribes-predicted-the-weather/.

Cartier, K. M. S. (2021, October 8). Keeping indigenous science knowledge out of a colonial mold. Eos. Retrieved December 8, 2021, from https://eos.org/articles/keeping-indigenous-science-knowledge-out-of-a-colonial-mold.

Ceolato, R., & Berg, M. J. (2021). Aerosol Light Extinction and backscattering: A review with a lidar perspective. Journal of Quantitative Spectroscopy and Radiative Transfer, 262, 107492. https://doi.org/10.1016/j.jqsrt.2020.107492

Chugach Heritage. (n.d.). Traditional weather forecasting - Chugachmiut heritage preservation. Chugach Heritage. Retrieved December 8, 2021, from https://chugachheritageak.org/traditional-weather-forecasting.

David-Chavez, D. M., Valdez, S., Estevez, J. B., Meléndez Martínez, C., Garcia, A. A., Josephs, K., & Troncoso, A. (2020). Community-based (rooted) research for regeneration: Understanding benefits, barriers, and resources for Indigenous Education and Research. AlterNative: An International Journal of Indigenous Peoples, 16(3), 220–232. https://doi.org/10.1177/1177180120952896

Donovan, D. P., & van Lammeren, A. C. (2001). Cloud effective particle size and water content profile retrievals using combined Lidar and RADAR OBSERVATIONS: 1. theory and examples. Journal of Geophysical Research: Atmospheres, 106(D21), 27425–27448. https://doi.org/10.1029/2001jd900243

Dorf, R. C. (2014). The Electrical Engineering Handbook. CRC Press.

Duforêt-Gaurier, L., Moutier, W., Guiselin, N., Thyssen, M., Dubelaar, G., Mériaux, X., Courcot, L., Dessailly, D., & Loisel, H. (2015). Determination of backscattering cross section of individual particles from cytometric measurements: A new methodology. Optics Express, 23(24), 31510. https://doi.org/10.1364/Bouroe.23.031510

Düsing, S., Ansmann, A., Baars, H., Corbin, J. C., Denjean, C., Gysel-Beer, M., Müller, T., Poulain, L., Siebert, H., Spindler, G., Tuch, T., Wehner, B., & Wiedensohler, A. (2021). Closure of in-situ measured aerosol backscattering and extinctioncoefficients with lidar accounting for relative humidity. https://doi.org/10.5194/acp-2021-21

Foot, J. S. Some observations of the optical properties of clouds. I: Stratocumulus, Q.J.R. Meteorol. Soc., 114, 129-144, 1988

Geisinger, A., Behrendt, A., Wulfmeyer, V., Strohbach, J., Förstner, J., & Potthast, R. (2017). Development and application of a backscatter lidar forward operator for quantitative validation of aerosol dispersion models and future data assimilation. Atmospheric Measurement Techniques, 10(12), 4705–4726. https://doi.org/10.5194/amt-10-4705-2017

The highs and lows of air pressure. The Highs and Lows of Air Pressure — UCAR Center for Science Education. (n.d.). Retrieved December 8, 2021, from https://scied.ucar.edu/learning-zone/how-weather-works/highs-and-lows-air-pressure#: :text=A%20low%20pressure%20syste

How do high and low weather systems work? ABC (Australian Broadcasting Corporation). (2013, January 30). Retrieved December 8, 2021, from https://www.abc.net.au/

science/articles/2013/01/31/3679358.htm.

Hadley cells. (n.d.). Retrieved December 21, 2021, from https://groups.seas.harvard .edu/climate/eli/research/equable/hadley.html

Jurányi, Z., & Weller, R. (2019). One year of aerosol refractive index measurement from a coastal Antarctic site. Atmospheric Chemistry and Physics, 19(22), 14417–14430. https://doi.org/10.5194/acp-19-14417-2019

Meteo 300, 6.12 what about scattering? — METEO 300: Fundamentals of Atmospheric Science. (n.d.). Retrieved December 8, 2021, from https://www.e-education.psu.edu/meteo300/

Mishchenko, M. L., Travis, L. D., and Lacis, A. A.: Scattering, absorption, and emission of light by small particles, Cambridge University Press, ISBN 0-521-78252-X, 448 pp., 2002.

Probert-Jones Equation. 35. the radar equation. (n.d.). Retrieved December 8, 2021, from http://www.geosci.sfsu.edu/geosciences/classes/m415_715/Monteverdi /Radar/RadarEquation/decibels.htm#: :text=Probert%2DJones%20Equation&text= (Attenuation%20is%20the%20weakening%20of,is%20mm6m%2D3.&text=For%20example%2 C%20if%20Z%20%3D%204000,10%20x%203.6%20%3D%2036%20dBZ.

Sicard, M., Rodríguez-Gómez, A., Comerón, A., & Muñoz-Porcar, C. (2020). Calculation of the overlap function and associated error of an elastic lidar or a ceilometer: Cross-comparison with a cooperative overlap-corrected system. Sensors, 20(21), 6312. https://doi.org/10.3390/s20216312

Springer. (2014). Lidar.

Thompson, M. T. (2006). Review of Diode Physics and the ideal (and later, nonideal) diode. Intuitive Analog Circuit Design, 43–74. https://doi.org/10.1016/b978-075067786-8/50003-3

Wang, Z., Borovoi, A., Konoshonkin, A., Kustova, N. V., Wang, B., Wu, D., Liu, D., Xie, C., & Wang, Y. (2020). The polarization characteristics of Cirrus Cloud using LIDAR and Radar in Hefei. 26th International Symposium on Atmospheric and Ocean Optics, Atmospheric Physics. https://doi.org/10.1117/12.2575821